

Enhancing corrosion resistance through crystallographic texture control in additively manufactured superelastic NiTi alloy

Zhu, Jia Ning; Li, Ziyu; Rahimi, Ehsan; Yan, Zhaorui; Ding, Zhaoying; Mol, Arjan; Popovich, Vera

DOI

[10.1016/j.corsci.2025.112929](https://doi.org/10.1016/j.corsci.2025.112929)

Publication date

2025

Document Version

Final published version

Published in

Corrosion Science

Citation (APA)

Zhu, J. N., Li, Z., Rahimi, E., Yan, Z., Ding, Z., Mol, A., & Popovich, V. (2025). Enhancing corrosion resistance through crystallographic texture control in additively manufactured superelastic NiTi alloy. *Corrosion Science*, 251, Article 112929. <https://doi.org/10.1016/j.corsci.2025.112929>

Important note

To cite this publication, please use the final published version (if applicable). Please check the document version above.

Copyright

Other than for strictly personal use, it is not permitted to download, forward or distribute the text or part of it, without the consent of the author(s) and/or copyright holder(s), unless the work is under an open content license such as Creative Commons.

Takedown policy

Please contact us and provide details if you believe this document breaches copyrights. We will remove access to the work immediately and investigate your claim.



Enhancing corrosion resistance through crystallographic texture control in additively manufactured superelastic NiTi alloy

Jia-Ning Zhu , Ziyu Li ^{*} , Ehsan Rahimi , Zhaorui Yan ^{*} , Zhaoying Ding, Arjan Mol , Vera Popovich

Department of Materials Science and Engineering, Delft University of Technology, Mekelweg 2, Delft 2628, the Netherlands

ARTICLE INFO

Keywords:

NiTi alloy
Corrosion
Additive manufacturing
Crystallographic texture

ABSTRACT

NiTi alloys, widely used for their shape memory and superelastic properties, face corrosion challenges when fabricated via laser powder bed fusion (LPBF). This study investigates the dual-phase formation in LPBF NiTi and its impact on corrosion resistance. Thermal simulations and microstructural analysis reveal that thermal stress drives martensite formation near melt pool boundaries. Martensitic regions act as anodic sites, leading to localized corrosion. Optimizing LPBF parameters produced single-phase [001]-textured NiTi, eliminating martensite and significantly reducing the corrosion current by almost two orders of magnitude and enhancing superelastic performance simultaneously. These findings highlight texture control as a key strategy to improve corrosion resistance and functionality for advanced applications.

1. Introduction

Laser Powder Bed Fusion (LPBF) has become a widely used additive manufacturing technique for fabricating nickel-titanium (NiTi) alloys [1], offering advantages, including the ability to create complex geometries with high precision [2] and to tailor their microstructure *in-situ* [3, 4]. The flexibility of tuning processing parameters in LPBF can significantly affect NiTi functionalities, such as superelasticity [3], shape memory effect, and phase transformation behavior [5]. These characteristics make LPBF an attractive option for manufacturing NiTi components, especially for high-performance applications in fields such as medical devices, aerospace, and robotics, where material properties and design flexibility are critical [1].

By adjusting the key LPBF processing parameters such as laser power, scanning speed, hatch distance (adjacent laser spacing), and beam shape, researchers have successfully tailored the crystallographic textures, microstructures, and phase transformation behavior of LPBF-processed NiTi to achieve desirable functional properties [5–7]. For instance, Xue *et al.* demonstrated that LPBF NiTi exhibits superior superelasticity [8], while other studies have shown that phase transformation behavior and cyclic stability can be better controlled through careful adjustment of the processing conditions and post treatments [9].

Recently, the corrosion behavior of LPBF NiTi has received increased attention alongside its mechanical properties, as it is a critical factor for

industrial applications. In environments such as seawater and harsh chemical settings [10], NiTi alloys are commonly used in dampers, sensors, and actuators [11]. However, these applications expose the NiTi alloys to corrosive environments that can compromise their structural integrity and long-term reliability.

Previous studies have reported the distinct corrosion behavior in LPBF NiTi. For example, Qiu *et al.* [12] found that the plane perpendicular to the building direction has better corrosion resistance than the plane parallel to the building direction. This difference arises from the unique microstructure of LPBF NiTi, which consists of columnar grains. The smaller grain size in the plane perpendicular to the building direction promotes the formation of a more uniform passive film, while the larger and uneven grains along the building direction result in non-uniform passive films. Furthermore, XRD and EBSD studies have shown that various laser power results in dual phase (mixed phases of austenite and martensite) or single austenitic phase in NiTi [13]. The dual phase regions lead to uneven passive film formation, and pitting corrosion tends to occur on these irregular surfaces [13].

Despite these findings, the corrosion mechanism of LPBF NiTi is still not fully understood. It is unclear why the presence of mixed austenite and martensite phases results in reduced corrosion resistance compared to single-phase austenitic NiTi [13]. Furthermore, the corrosion process in mixed-phase regions, as well as the reasons for the formation of these phases during LPBF, remain unanswered. Addressing these gaps is

^{*} Corresponding authors.

E-mail addresses: Z.Li-12@tudelft.nl, zyli16@163.com (Z. Li), Z.YAN-1@tudelft.nl (Z. Yan).

<https://doi.org/10.1016/j.corsci.2025.112929>

Received 31 January 2025; Received in revised form 19 March 2025; Accepted 5 April 2025

Available online 7 April 2025

0010-938X/© 2025 The Author(s). Published by Elsevier Ltd. This is an open access article under the CC BY license (<http://creativecommons.org/licenses/by/4.0/>).

crucial for enhancing the performance and reliability of LPBF NiTi in industrial applications.

To investigate these issues, this study explores the corrosion behavior of LPBF NiTi using multiscale characterization techniques. The present study aims to thoroughly investigate the corrosion mechanism of LPBF NiTi and explore effective strategies to enhance its anti-corrosion properties. In microstructural and crystallographic analysis, scanning electron microscopy (SEM) equipped with electron backscatter diffraction (EBSD) was utilized to examine the microstructure, texture, and phase distribution of LPBF NiTi. Transmission electron microscopy (TEM) was employed to analyze dislocation structures and low angle grain boundaries. For electrochemical characterization, electrochemical impedance spectroscopy (EIS) measurements followed by potentiodynamic polarization (PDP) were carried out to evaluate the corrosion resistance. Scanning Kelvin probe force microscopy (SKPFM) was used to analyze the surface potential distribution. Additionally, X-ray photoelectron spectroscopy (XPS) was applied to analyze the chemical composition of the passive film.

2. Materials and methods

2.1. Materials fabrication

NiTi samples were fabricated using an SLM 250HL machine via laser powder bed fusion (LPBF). Dual-phase samples were produced with a laser power of 400 W, scanning speed of 1250 mm/s, hatch spacing of 120 μm , and powder layer thickness of 30 μm . The [001]-textured samples were fabricated using a laser power of 950 W, scanning speed of 650 mm/s, hatch spacing of 180 μm , and powder layer thickness of 40 μm . A stripe scanning strategy with a rotation of 67.5° between layers was employed. High-purity argon gas was used to prevent oxidation during fabrication. The feedstock was commercial Ni_{51.4}Ti_{48.6} powder with spherical morphology, fabricated via gas atomization, and characterized by particle size distributions of 23 μm (D10), 40 μm (D50), and 67 μm (D90).

To investigate corrosion behavior and compressive superelasticity, as-fabricated cylindrical samples of 13 mm diameter and 25 mm height (along the building direction) were built and then machined into eight compressive cuboids (4 × 4 × 8 mm³) using electrical discharge machining (EDM). For differential scanning calorimetry (DSC) measurement, samples were machined by EDM with a dimension of 4 × 4 × 1 mm³. All samples were ground and polished according to standard metallographic procedures unless otherwise stated.

2.2. Microstructure characterization

Microstructure, texture, and phase analysis were conducted using a scanning electron microscope (SEM, Helios G4) equipped with an electron backscatter diffraction (EBSD) detector. The samples for EBSD analysis were first mechanically ground and polished to a final grit size of 1 μm . To eliminate residual stress introduced during mechanical polishing, which could potentially induce stress-induced martensite, electropolishing was performed using an A3 electrolyte (Struers) in a LectroPol-5 electrolytic polishing machine. The electropolishing process was conducted at a voltage of 10 V for 10 seconds at a temperature of 8°C. Samples after electrochemical impedance spectroscopy (EIS) and potentiodynamic polarization (PDP) tests were directly subjected to EBSD analysis without additional surface preparation. It should be noted that, to the best of our knowledge, this is the first conclusive identification of martensite in NiTi fabricated via LPBF by EBSD. In earlier investigations, suboptimal sample preparation and the inherent difficulty of indexing the monoclinic martensite phase may have caused some martensitic regions to be classified as non-indexed [14,15]. EBSD data were collected at 30 kV with 13 nA current and analyzed using OIM Analysis software. High-resolution EBSD with a step size of 200 nm was employed to resolve fine martensitic phases, determine crystallographic

texture, and identify grain boundary characteristics. Kernel Average Misorientation (KAM) maps were generated to assess localized strain distribution, while phase maps distinguished between austenitic (B2) and martensitic (B19') phases.

Transmission electron microscopy (TEM) was employed to analyze dislocation structures and low-angle grain boundaries. TEM samples were fabricated using a Helios G4 PFIB and observed with a Titan 80–300ST TEM (FEI) at an acceleration voltage of 300 kV. Selected area electron diffraction (SAED) was performed to confirm crystallographic orientations and grain boundary characteristics.

2.3. Electrochemical characterization

EIS measurements, followed by potentiodynamic polarization (PDP), were performed after 1 h immersion in a 3.5 wt% NaCl solution. A traditional three-electrode system was employed in this study. A NiTi alloy coupon served as the working electrode. The exposed surface was created by covering the working electrode surfaces using a water-proof tape with a round hole of 3 mm diameter. An Ag/AgCl/KCl 3 M reference electrode (+222 mV vs. SHE) was used as the reference electrode, and a platinum mesh functioned as the counter electrode. The NiTi electrode was ground up to grit 4000 SiC abrasive paper, polished using 3 μm and 1 μm alumina slurry, then gently cleaned with distilled water and dried through compressed air. Adhesive copper tape was used for electrical connection between the NiTi alloy and the potentiostat. The EIS measurements were conducted in the frequency range from 100 kHz to 0.01 Hz by applying a ± 10 mV sinusoidal excitation signal by a Biologic SP 300 multichannel potentiostat. The fitting process of all EIS data was conducted using Zview software. The PDP curves were recorded from -200 mV to $+1.5$ V vs. OCP with a scanning rate of 1 mV/s.

2.4. Scanning Kelvin probe force microscopy measurements

Scanning Kelvin probe force microscopy (SKPFM) measurements were performed using a Bruker Dimension Edge™ instrument with Nanodrive v8.05 software. Samples were measured in the as-received state. The surface potential images were obtained by a dual-scan mode: in the first scan, topography data were collected using a tapping mode, and in the second scan, the surface potential was measured by lifting the tip up to 50 nm. Topography and surface potential measurements were conducted in ambient atmosphere at 22 ± 1 °C, with a zero-bias voltage, a pixel resolution of 512×512 , a scanning area of $100 \times 50 \mu\text{m}^2$, and a scan frequency rate of 0.3 Hz. The raw data was analyzed using Gwyddion 2.60 software. A histogram analysis based on the multimodal Gaussian distributions was performed to represent the surface potential distribution between different regions.

2.5. X-ray photoelectron spectroscopy

X-ray photoelectron spectroscopy (XPS) measurements were conducted to analyze the chemical composition and relative fractions of the formed (hydro)oxide layers after 1 hour of exposure to 3.5 % NaCl in an ambient environment. The XPS analysis was conducted using a PHI-Versaprobe II (Physical Electronics) spectrometer equipped with a monochromatic Al K α X-ray source (1486.6 eV photon energy) and automatic neutralizer. The binding energy range was calibrated using the Cu 2p_{3/2} (932.62 ± 0.1 eV) and Au 4f_{7/2} (83.96 ± 0.1 eV) reference lines. Spectra were recorded at a takeoff angle of 45° with an irradiation power of 49.6 W, corresponding to a beam diameter of 200 μm . The samples were mounted onto the specimen holder using double-sided tape to electrically isolate it from the ground. Measurements were conducted using the built-in charge neutralizing system, which combines low-energy electrons and an ion beam. Calibration of the system was performed using a PET reference sample, with the full width at half maximum (FWHM) of the O=C–O C 1 s peak maintained below 0.85 eV. High-resolution scans of the O 1 s, Ti 2p, Ni 2p, and C 1 s regions were

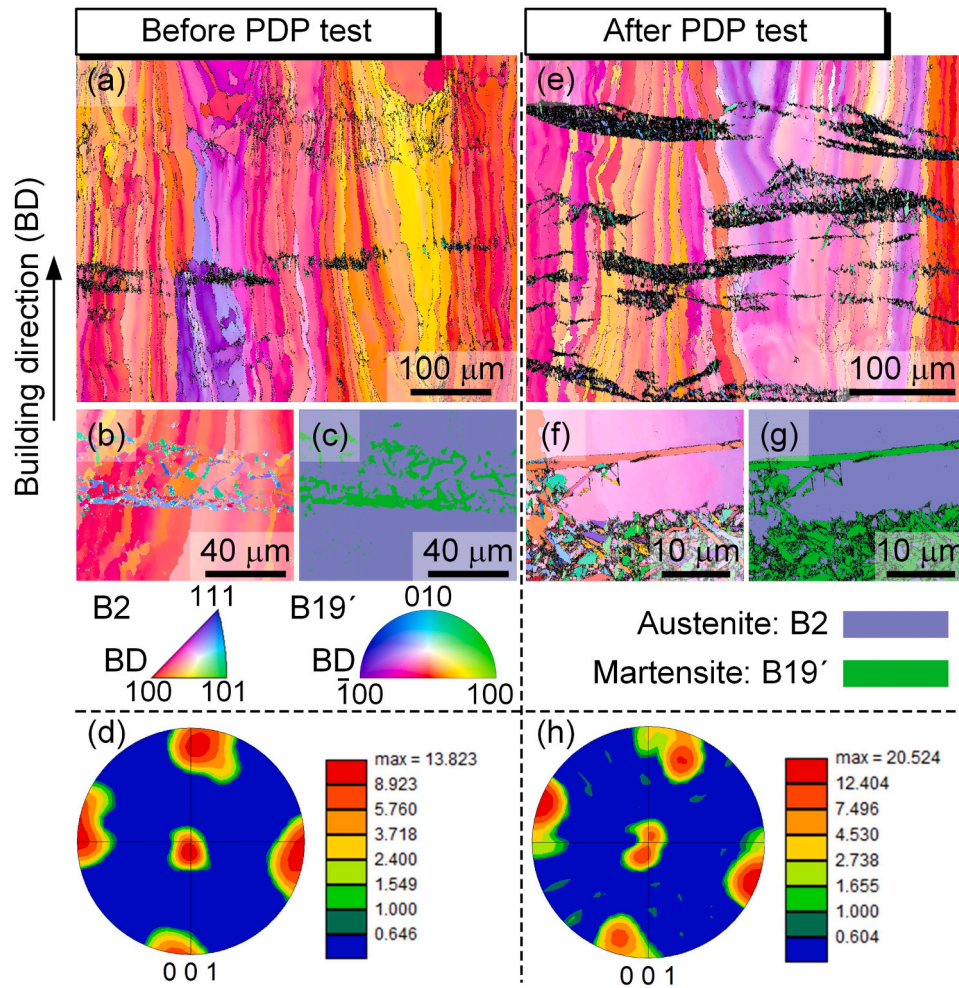


Fig. 1. LPBF dual-phase NiTi samples before and after PDP tests. (a) Orientation map along the building direction (BD) before PDP, showing non-indexed (black colored) regions near melt pool boundaries. (b, c) High-resolution EBSD maps with a step size of $0.5 \mu\text{m}$ highlighting martensitic phases (hence with resolved previously non-indexed regions) before PDP. (d) A pole figure of dual-phase NiTi before PDP test. (e) Orientation map along the building direction after corrosion, showing similar non-indexed regions near melt pool boundaries. (f, g) High-resolution EBSD maps after PDP, confirming the presence of martensitic phases. Austenitic (B2) and martensitic (B19') phases are represented in blue and green, respectively. (h) A pole figure of dual-phase NiTi after PDP.

acquired using a pass energy of 23 eV, a step size of 0.1 eV, and a dwell time of 50 ms per step. The chamber pressure during measurements was maintained at approximately $\sim 7.5 \times 10^{-9}$ Torr due to the inflow of Ar ions used for neutralization. All spectra were charge-corrected with respect to the adventitious carbon C 1 s peak, which was set at 284.8 eV. Data analysis was performed using PHI Multipack software (V9.9.2).

2.6. Melt pool simulation

The temperature distribution and gradients in the melt pool during LPBF processing were simulated using ABAQUS. Details of the melt pool calculations are provided in previous work [16].

2.7. Superelastic tests

Superelasticity was tested on an MTS 858 tabletop hydraulic test machine by applying uniaxial compression. A strain rate of $1.0 \times 10^{-4} \text{ s}^{-1}$ was applied and strains were measured by a contact-based ceramic extensometer (632.53F-14, MTS). The test temperatures are set to be 10 K above the austenite finish temperature. For dual-phase samples, the austenite finish temperature is 327 K. For the [001]-textured sample, the austenite finish temperature is 295 K. Both austenite finish temperatures were measured by DSC (PerkinElmer DSC 8000).

3. Results and discussion

3.1. Microstructure and crystallographic texture

Fig. 1 presents the crystallographic texture and phase distribution of LPBF dual-phase NiTi samples before and after PDP testing (the PDP results will be presented later). No pronounced differences are observed between the two conditions, as validated by pole figures in Fig. 1(d) and (h). For the austenitic phase, the sample shows a mixed texture consisting of [001] orientated grains and other randomly orientated grains. Both samples exhibit non-indexed regions, which are primarily located near the melt pool boundaries, as shown in Fig. 1(a) and (e). These non-indexed regions are associated with the martensitic phases. The martensitic phases in these regions were difficult to index due to their fine size and complex morphology. The varying area fractions of non-indexed martensite observed in EBSD before and after PDP tests are due to the inhomogeneous microstructure present in different locations of the dual-phase NiTi (Fig. 1(a) and (e)). The application of high-resolution EBSD with a small step size of 200 nm successfully resolved and indexed these features. Fig. 1(b) and 1(c) highlight the indexed martensitic phases and their distribution before PDP. Similarly, Fig. 1(f) and 1(g) illustrate these features after PDP. The consistent appearance of non-indexed regions, particularly those identified near melt pool boundaries (Fig. 1(b)), and their identification as martensite indicate

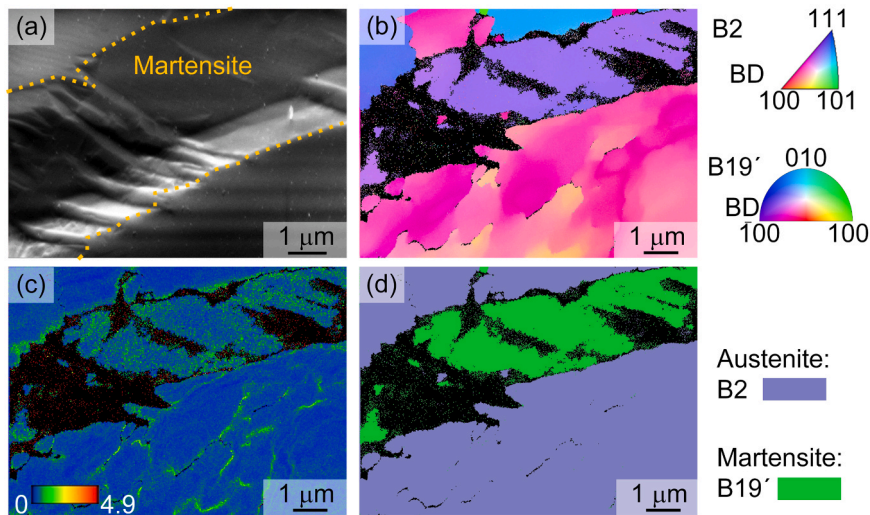


Fig. 2. Microstructure and EBSD analysis of the martensitic phase in LPBF dual-phase NiTi before corrosion. (a) Microstructural image showing the typical martensite morphology with sharp interfaces. (b) Orientation map indicating the distribution of B2 (austenite) and B19' (martensite). (c) Kernel Average Misorientation (KAM) map showing localized lattice distortion in the martensitic phase. (d) Phase map confirming the clear interface between austenite (blue) and martensite (green).

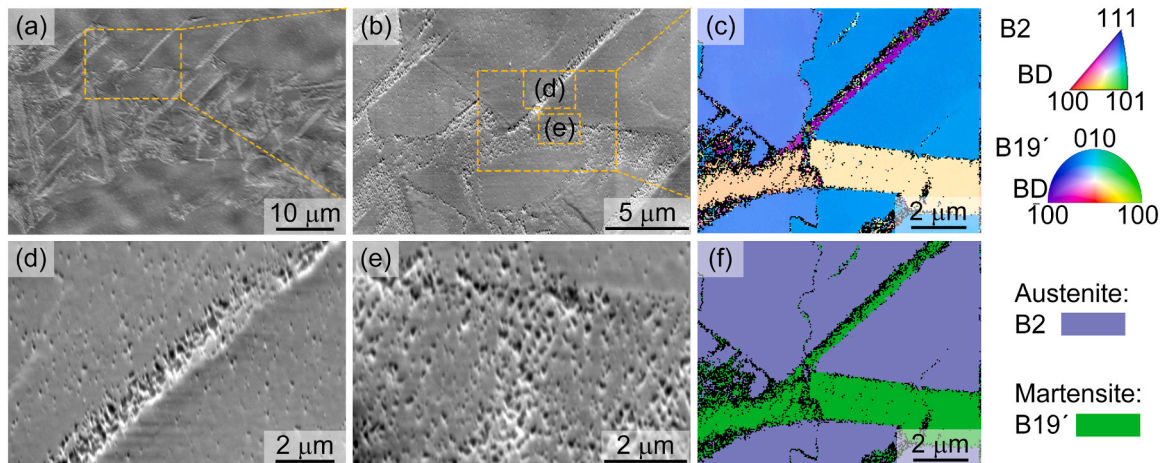


Fig. 3. Microstructural features and EBSD analysis of LPBF dual-phase NiTi after the corrosion test. (a, b) Surface morphology showing corrosion pits in both B2 (austenite) and B19' (martensite) phases. (c) Orientation map indicating the distribution of B2 and B19' phases in the corroded area. (d, e) Magnified views of corrosion pits. (f) Phase map showing austenite and martensite. Note that the same sample (as used in Fig. 2) was used to compare the differences before and after EIS, followed by PDP tests.

that these features are inherent to the microstructure of LPBF NiTi and remain unaffected by the PDP.

To determine the corrosion mechanism, the high-resolution microstructure and EBSD results have been correlated before and after electrochemical measurements. Fig. 2 provides detailed insights into LPBF dual-phase NiTi before electrochemical tests in NaCl solution. In Fig. 2 (a), the martensitic phase is observed with a clear morphology and twin-type feature, characteristic of typical martensite. This morphology is outlined in the microstructural image, highlighting the localized distribution of the martensite. Fig. 2(b)–(d) present an EBSD analysis of the same region. Fig. 2(b) shows the orientation map, where the B2 (austenite) and B19' (martensite) phases are clearly distinguished. Fig. 2 (c) provides the KAM map, indicating local misorientation primarily in the martensitic phase and grain boundaries of austenitic grains. Fig. 2(d) highlights the phase map, confirming the clear interfaces between austenite (blue) and martensite (green).

To better understand where and how corrosion occurs, the LPBF dual-phase NiTi sample was closely examined after the EIS and PDP

tests. As shown in Fig. 3(a) and 3 (b), pitting is visible on both the B2 (austenite) and B19' (martensite) phases. At higher magnification, the B19' phase shows more severe corrosion, with dense pits compared to the B2 phase (Fig. 3(d) and (e)). This suggests that the B19' phase has lower corrosion resistance under the PDP test conditions. The EBSD orientation map (Fig. 3(c)) and phase map (Fig. 3(f)) clearly indicate where the pits are located in the two phases. The difference in corrosion severity may be due to an electrochemical potential difference between the B2 and B19' phases. The B19' phase might act as a sacrificial part (active and high energy site), corroding faster than the B2 phase.

3.2. Electrochemical properties of the LPBF dual-phase NiTi

To visualize the differences in electrical surface potential distribution between the B2 (austenite) and B19' (martensite) phases, SKPFM measurements were performed. Fig. 4(a)–4(c) presents the AFM topography, amplitude, and SKPFM images of the LPBF dual-phase sample, separately. The topography image in Fig. 4(a) reveals a smooth surface,

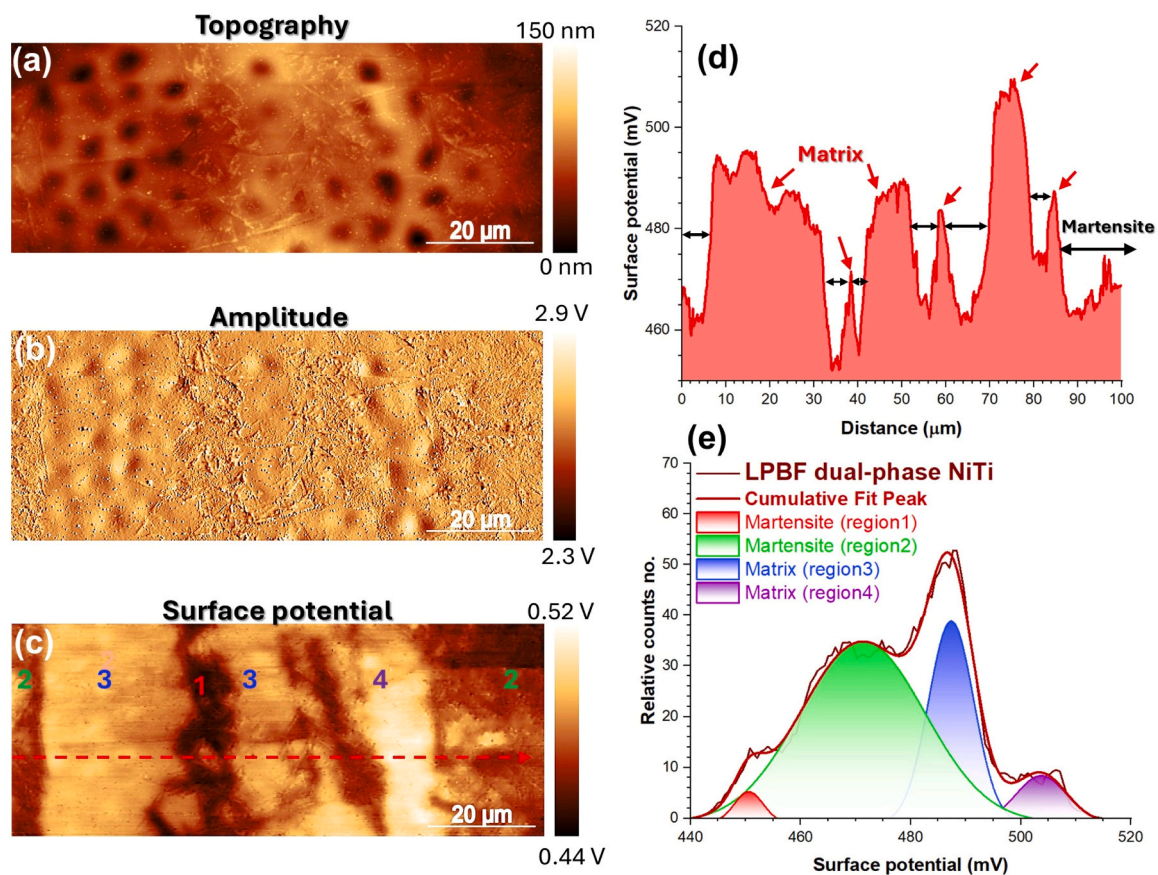


Fig. 4. (a) AFM topography, (b) Amplitude, (c) SKPFM map of the LPBF dual-phase NiTi, (d) Volta potential linear profiles of the LPBF dual-phase NiTi, (e) histogram plot of the SKPFM image and its de-convolution using simulated multinomial Gaussian distribution for LPBF dual-phase NiTi.

with the spot-like features resulting from electrolytic polishing. The amplitude image in Fig. 4(b) clearly distinguishes between the austenite and martensite phases, with the martensitic region comprising needle-like, small-sized martensite phases. The surface potential mapping demonstrates that the presence of martensite generates lower and more heterogeneous (Fig. 4e) surface potential distribution, with the martensitic phase distinctly recognized as dark regions in Fig. 4(c). The linear potential profile marked in Fig. 4(c) is presented in Fig. 4(d), where the line scan of the LPBF dual-phase sample reveals pronounced oscillations (black-wide arrows). Regions 1 and 2 (also in the histogram), appearing darker, correspond to the martensitic phase, while the adjacent lighter areas represent the austenitic matrix (regions 3 and 4). SKPFM can measure the electron work function of metal surfaces in vacuum or air conditions and work function variations among

microstructural features cause noticeable shifts in surface potential across the surface, offering insights into their anodic and cathodic electrochemical properties [17–19]. Previous studies have demonstrated a strong correlation between the corrosion potential at the solid/liquid interface and the measured electrical surface potential at the solid/air interface within the scanned area [18,20–22]. Nevertheless, establishing a direct correlation between these potentials and the electrochemical behaviour in actual corrosion scenarios often proves challenging [19] and needs to be substantiated by actual electrochemical analysis under representative corrosive conditions as is done in this study. Typically, noble materials exhibit a higher work function compared to relatively electrochemically active materials [23,24]. Consequently, a higher surface potential, as measured by SKPFM, suggests more noble electrochemical properties under aqueous electrolyte

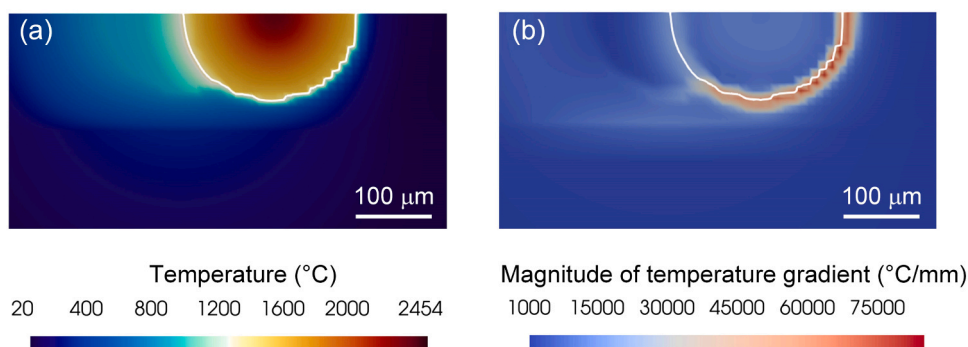


Fig. 5. Thermal behaviors of the melt pool during LPBF processing of dual phase LPBF NiTi: (a) Temperature distribution and (b) Magnitude of temperature gradient. The melt pool boundaries are marked by white solid lines (Melting point is 1310 °C).

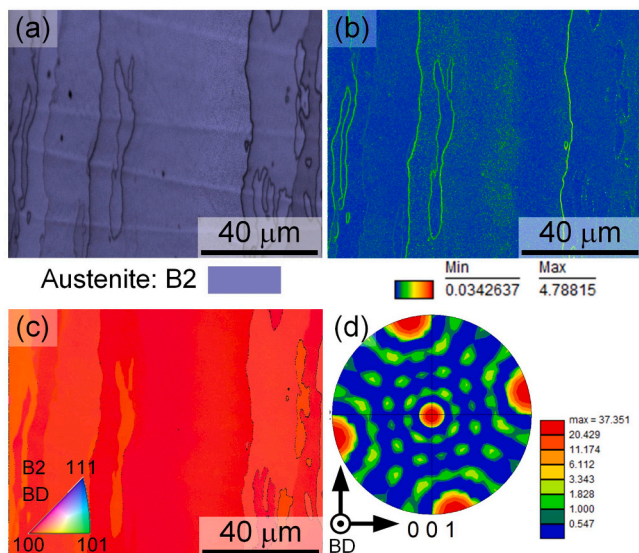


Fig. 6. Microstructural and crystallographic analysis of [001]-textured single-phase LPBF NiTi. (a) Phase map showing the single austenitic (B2) phase distribution. (b) KAM map highlighting uniform strain distribution within the microstructure. (c) IPF map revealing a strong [001] texture along the building direction (BD). (d) A Pole figure confirming the pronounced [001] single-crystal-like texture with high alignment along the BD.

conditions. This surface potential variation can serve as a predictive indicator of corrosion behaviour [25]. Therefore, the SKPFM results indicate that the martensitic phase acts as the anodic site, which aligns with the SEM observations after PDP testing (Fig. 3). To better quantify the galvanic driving force (ΔV), an enlarged view of the scanned area of the LPBF dual-phase sample is provided in Figure S1, showing an approximate value of 50 mV. Regions with a lower surface potential are more susceptible to acting as anodic sites (more electrochemical activity) in a galvanic coupling.

However, the selection of line profiles is often subjective, which may introduce errors. Therefore, a statistical analysis is performed based on multiple line scan results. A histogram is shown in Fig. 4(e) to reveal the influence of different phases on the surface potential distribution [18, 26]. The histogram profile of the LPBF dual-phase NiTi surface can be resolved into four peaks: two associated with martensite and two with austenite (matrix). This demonstrates significant surface potential heterogeneity, with martensitic regions consistently showing lower average potential values compared to austenitic regions.

3.3. The formation mechanism of dual phase in LPBF NiTi

As discussed in the Sections 3.1 and 3.2, the martensitic phase acts as the anodic site in the LPBF dual-phase NiTi. While the dual-phase microstructure in LPBF NiTi has been reported by Chen et al. [13] its formation mechanism remains unclear. Two hypotheses can be proposed to explain this phenomenon. The first hypothesis suggests that Ni evaporation during LPBF increases the phase transformation temperature above room temperature, causing regions with higher Ni evaporation to transform into martensite upon cooling [27]. The second hypothesis attributes the formation of dual phases to stress-induced martensitic transformation driven by residual stress after cooling, which results from strain compatibility during the L-PBF process [28].

To investigate the thermal effects on dual-phase formation, the temperature distribution and magnitude of the temperature gradients in the melt pool were simulated. The results are shown in Fig. 5. As shown in Fig. 5(a), the maximum temperature of the melt pool exceeds 2400 °C at the melt pool center. The temperature gradually decreases from the melt pool center to its boundary. As a consequence of depositing liquid

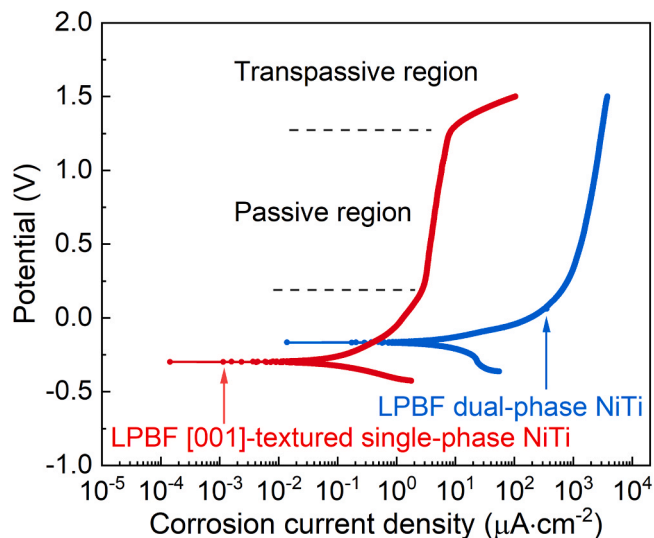


Fig. 7. PDP curves of both L-PBF NiTi samples after 1 h immersion in 3.5 wt% NaCl solution.

metal onto relatively cooler prior deposition layers, a steep temperature gradient forms at the outer boundary of the melt pool (Fig. 5(b)). This steep gradient induces significant thermal expansion of the solidified metal during heating and residual stress after cooling. To release these residual stresses, stress-induced martensitic transformation occurs, forming martensite at the outer boundary of the melt pool. Additionally, while the peak temperature near the melt pool center corresponds to regions with higher Ni evaporation, no martensite formation is observed near the center of the melt pool. These findings suggest that martensite formation near the melt pool boundary is primarily driven by the release of residual stresses.

3.4. A strategy for improving the corrosion resistance of LPBF NiTi

To address the challenges posed by the dual-phase microstructure in LPBF NiTi, particularly its adverse effects on corrosion resistance, the processing parameters were optimized to achieve a single-phase microstructure. As discussed in Section 3.3, the martensite phases, near the melt pool boundaries, result from thermal stress. The optimized processing parameters can reduce the temperature gradients and hence eliminate the stress-induced martensite [3]. Fig. 6(a) confirms the elimination of the martensitic phase, with the entire area indexed as the B2 phase. The KAM map (Fig. 6(b)) indicates that a larger misorientation is primarily found around grain boundaries, with some local strains within grains indicating the presence of dislocations. The IPF color map in Fig. 6(c) further illustrates the highly textured [001] direction along the building direction (BD), a feature resembling single-crystal-like behavior. The pole figure in Fig. 6(d) demonstrates a strong [001] texture, confirming the successful orientation alignment achieved through the modified processing parameters. Moreover, the SKPFM mapping shown in Figure S2 also proves that a more homogeneous surface potential distribution is realized after the removal of residual martensite.

To provide an overview of the electrochemical response and corrosion behaviour, the PDP curves of [001]-textured single-phase and dual-

Table 1
Potentiodynamic polarization parameter fitting values for LPBF dual-phase and [001]-textured single-phase NiTi samples.

Sample	E_{corr} (mV vs. Ag/AgCl)	i_{corr} ($\mu\text{A}\cdot\text{cm}^{-2}$)
LPBF dual-phase NiTi	-178 ± 5	10.60 ± 3.30
LPBF [001]-textured single-phase NiTi	-302 ± 4	0.09 ± 0.01

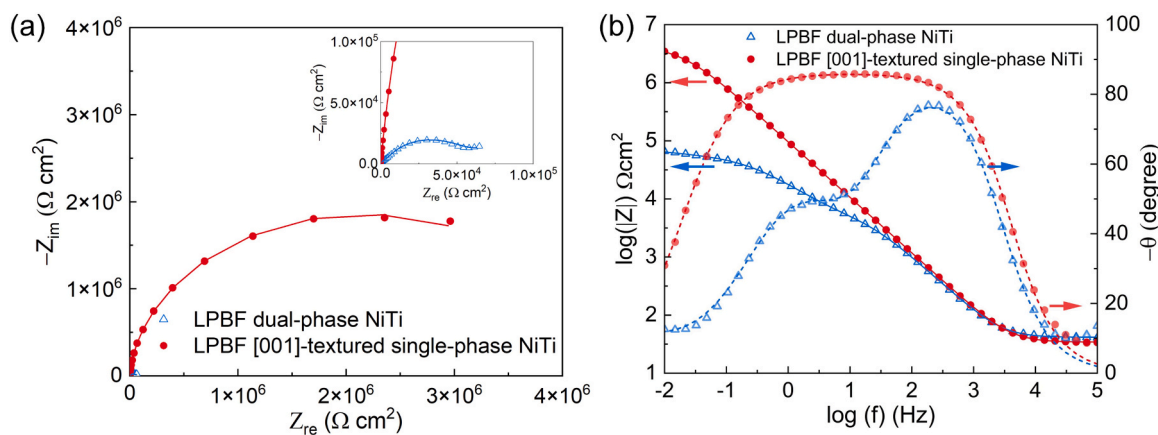


Fig. 8. Nyquist (a) and Bode (b) diagrams of the LPBF dual-phase and [001]-textured single-phase NiTi samples after immersion in 3.5 wt% NaCl solution for 1 h. The solid lines on top of the data represent fitting lines.

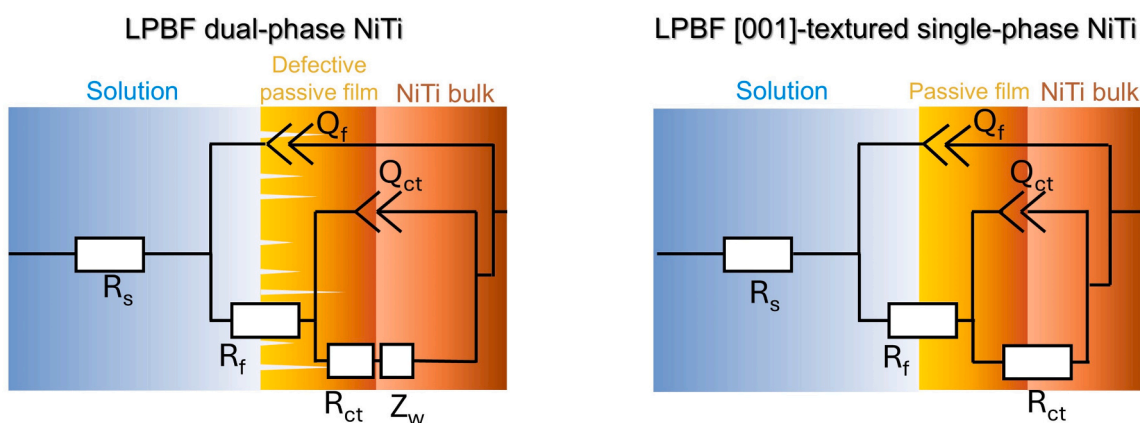


Fig. 9. Equivalent circuit of both L-PBF NiTi samples after immersion in 3.5 wt% NaCl solution for 1 h.

phase samples in a 3.5 % NaCl solution are compared in Fig. 7. Both NiTi samples exhibit a wide passivation plateau, without evident activation-passivation transition characteristics. The LPBF dual-phase NiTi exhibits a slightly higher corrosion potential (E_{corr}), around 125 mV, compared to the [001]-textured single-phase specimen. Nevertheless, its corrosion current density (i_{corr}) is almost 100 times higher than that of the [001]-textured single-phase NiTi sample. The fitting results from Tafel extrapolation are listed in Table 1. The i_{corr} of the [001]-textured single-phase specimen is less than $0.1\mu\text{A}\cdot\text{cm}^{-2}$, indicating the formation of a relatively well-protective passive film [29].

To compare the electrochemical interactions and corrosion resistance of passive films on LPBF dual-phase and [001]-textured single-phase NiTi samples, EIS spectra were obtained following 1 hour of immersion under open-circuit condition (OCP). Fig. 8(a) and (b) display the Nyquist and Bode plots of both NiTi alloys, respectively. The [001]-textured single-phase sample exhibits a significantly higher arc in its capacitance loop compared to the LPBF dual-phase NiTi. The broader and elevated phase angle further underscores its superior charge transfer resistance and enhanced corrosion performance. The phase angle in the

Bode diagram of the LPBF dual-phase NiTi sample exhibits two obvious capacitive arcs, indicating two-time constants [29]. Although the two-time-constant electrochemical response is not distinctly observable, the most accurate fitting was clearly identified in the [001]-textured single-phase NiTi sample (discussed in detail below). Moreover, a small tail can be observed on the Nyquist plot of the LPBF dual-phase NiTi sample at the low-frequency range, indicating that the diffusion process of ions takes place on the electrode. This might be attributed to a semi-finite thickness layer diffusion process in the relatively defective passive film of the LPBF dual-phase NiTi [30–32].

Therefore, two equivalent electrical circuits used for EIS parameters fitting of both samples are shown in Fig. 9. In this model, R_s indicates the resistance of the solution, R_{ct} is

the charge transfer resistance of the double-layer capacitor, Q_{dl} is a constant phase element (CPE) that reveals the charge separation between the metal and electrolyte interface, R_f is the resistance of the passive film, and Q_f is a CPE of the passive film. Z_w is the Warburg impedance which indicates the difficulty of mass transport of the redox species to the electrode surface under a semi-infinite linear diffusion.

Table 2

EIS parameters fitting values of the LPBF dual-phase (DP) and [001]-textured single-phase (SP) NiTi samples after immersion in 3.5 wt% NaCl solution for 1 h.

Sample	R_s Ωcm^2	$Q_f/10^{-6}$		R_f $\text{k}\Omega\text{cm}^2$	$Q_{ct}/10^{-6}$		R_{ct} $\text{k}\Omega\text{cm}^2$	Z_w	chi-squared
		$\frac{Y_0}{\Omega^{-1}\text{cm}^{-2}\text{s}^n}$	n		$\frac{Y_0}{\Omega^{-1}\text{cm}^{-2}\text{s}^n}$	n			
DP	41.5	2.1	0.95	5.8	12	0.75	48.1	81.3	0.0039
SP	35.1	1.8	0.96	3220	3.1	0.65	1328	-	0.0026

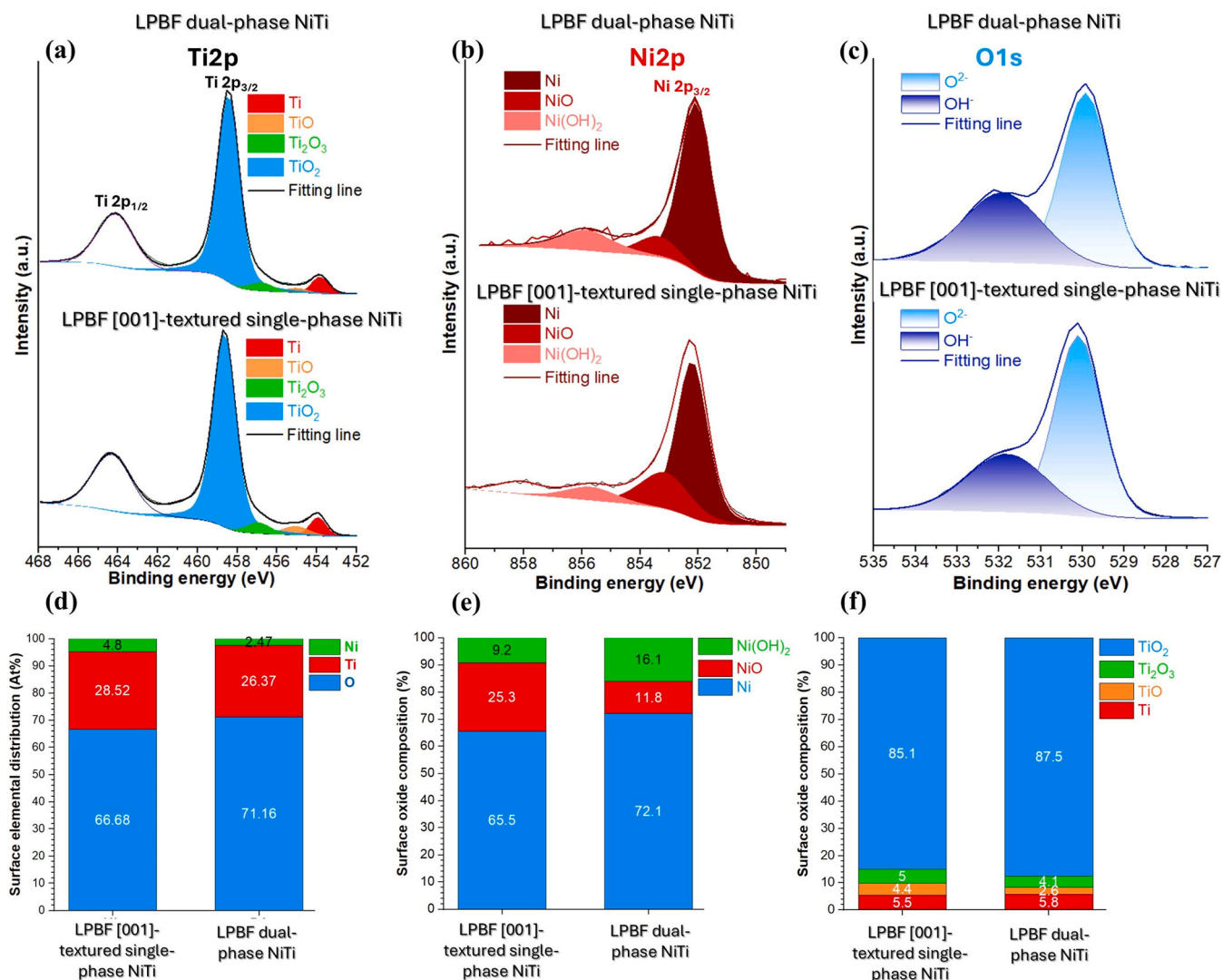


Fig. 10. XPS high-resolution spectra of the (a) Ti 2p, (b) Ni 2p, and (c) O 1s electron energy regions on both LPBF dual-phase and LPBF [001]-textured single-phase NiTi samples after exposure to the 3.5 % NaCl solution for 1 hour. (d) elemental distribution in surface bilayer oxide. The various oxidation states of (e) Ni and (f) Ti.

Considering that the capacitance is a non-ideal capacitor because of the roughness of the electrode surface and surface microstructural heterogeneity, CPE instead of capacitance is adopted [29]. The capacitance is related to the angular frequency of the excitation signal, which can be written as follows:

$$Z_{Qdl} = \frac{1}{Y_0(j\omega)^n} \quad (1)$$

where ω is the angular frequency, j is the symbol of an imaginary number, and n is the exponent of the CPE, usually ranging from 0.5 to 1. The fitting values of the equivalent electrical circuit elements are listed in Table 2. The fitted values demonstrate that the [001]-textured single-phase NiTi sample exhibits higher R_f and R_{ct} values compared to the LPBF dual-phase sample. This indicates enhanced corrosion resistance, aligning with the PDP results. Moreover, a lower capacitance value observed in the [001]-textured single-phase NiTi sample likely indicates the presence of a thicker and more compact passive film [29].

Previous studies have shown that TiO₂ is the primary composition of the passive film on NiTi alloy, providing effective corrosion protection to the substrate [33,34]. Liu *et al.* then further proved that the passive layer of NiTi alloy is a bilayer structure consisting of a Ti-rich outer layer and a Ni-rich inner layer [29]. Figs. 10(a)-(c) show high-resolution XPS spectra for Ti 2p, Ni 2p, and its associated O 1s signals, corresponding to

two different NiTi alloys. The Ti 2p spectra in Fig. 10(a) were deconvoluted into multiple components, revealing a minor presence of metallic Ti⁰ (453.8 eV), TiO (455.0 eV), and Ti₂O₃ (456.7 eV), alongside a predominant amount of TiO₂ oxidized state (458.4 eV).

By comparing the Ti oxidation states in the NiTi alloys shown in Fig. 10(f) with the surface elemental distribution in Fig. 10(d), slightly higher Ti and Ni contents are observable in the passive film of the [001]-textured single-phase. However, there is no significant difference in the various Ti oxidation states within the passive film composition between the two NiTi alloys. However, previous studies on NiTi alloys have shown that even slight variations in Ti oxidation states within the passive film can significantly impact the electrochemical stability and protective properties of the oxide layer, ultimately influencing corrosion resistance [12,29,35].

Fig. 10(b) indicates the high-resolution XPS spectra of the Ni 2p that deconvoluted into multiple components including metallic Ni⁰ (852.1 eV), NiO (853.3 eV), and Ni(OH)₂ (855.8 eV). By comparing the Ni oxidation states in the NiTi alloys presented in Fig. 10(e), a higher proportion of NiO and a lower amount of Ni(OH)₂ are observed in the [001]-textured single-phase alloy compared to the LPBF dual-phase alloy. This suggests improved charge transfer resistance in the inner layer of the bilayer oxide, as NiO oxide exhibits a higher work function ($\Phi_{NiO} = 6.3$ eV) than Ni(OH)₂ hydroxide ($\Phi_{Ni(OH)_2} = 3.88$ eV) [36,37].

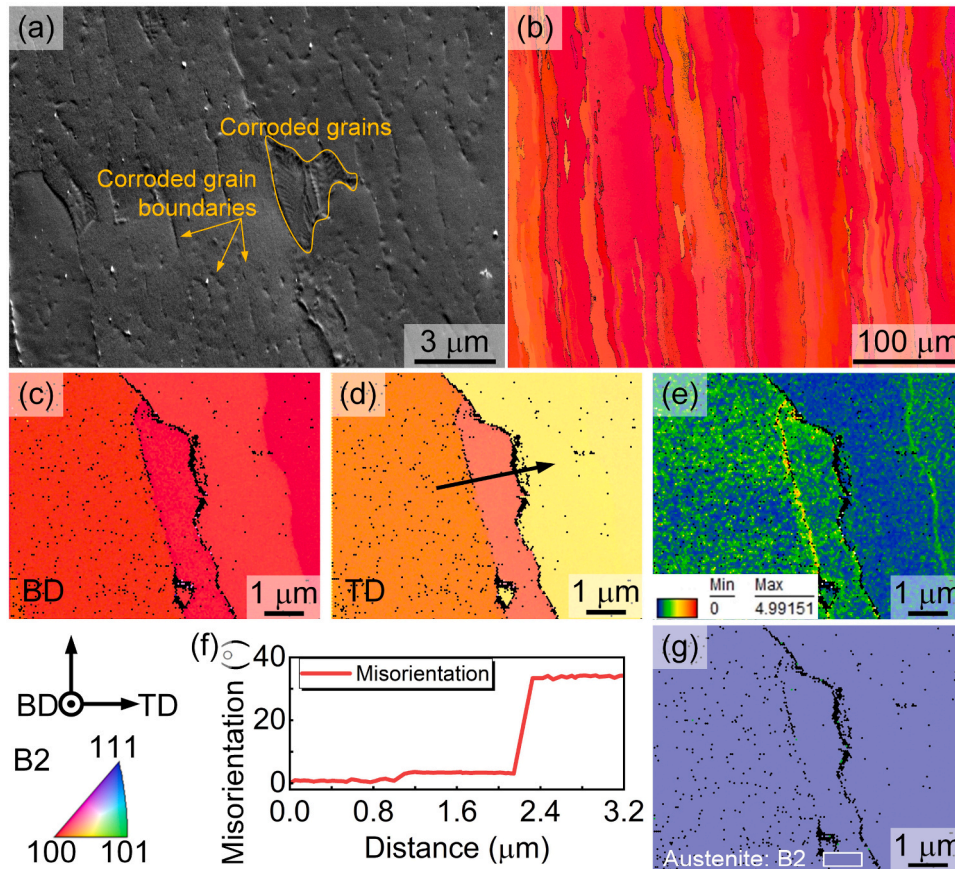


Fig. 11. Microstructural and crystallographic analysis of [001]-textured single-phase NiTi after corrosion testing. (a) SEM image showing corroded grains and grain boundaries. (b) Orientation map highlighting the [001] texture with a low magnification. (c, d) Orientation maps in the BD and TD, showing corroded regions at high-angle grain boundaries. (e) Kernel Average Misorientation (KAM) map indicating strain concentration at corroded boundaries. (f) Misorientation profile across a high-angle boundary (marked by a black arrow in (d)). (g) Phase map confirming the single-phase B2 structure. The elimination of martensite and reduction of high-angle grain boundaries significantly enhance the material's corrosion resistance.

Moreover, in this work, optimized manufacturing parameters not only lead to a slight increase in Ti and Ni content within the passive film but also introduce notable differences in the martensitic phase fraction. This change in microstructure plays a crucial role in corrosion behavior, as a

single-phase structure enhances the phase stability of NiTi alloys. As a result, the significant improvement in corrosion resistance observed here can be attributed to both the passive film composition and especially the stabilized microstructure.

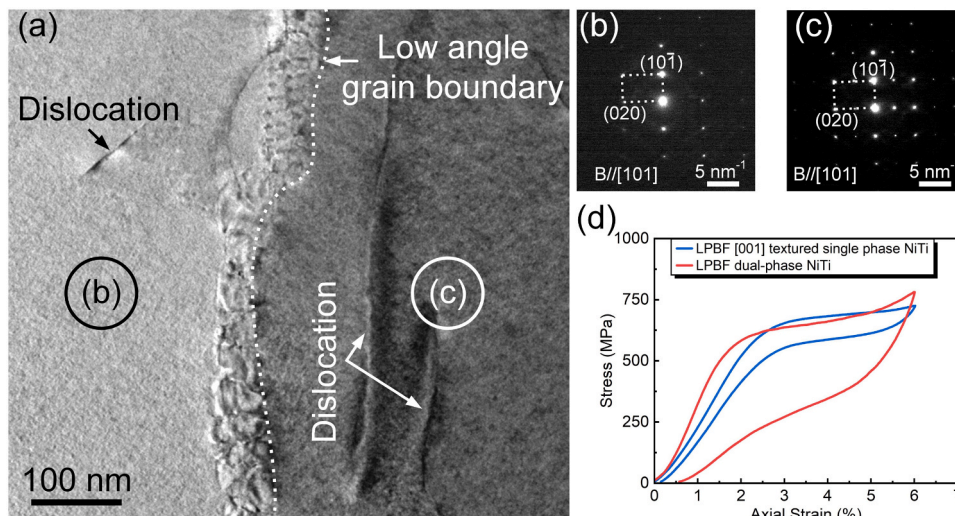


Fig. 12. TEM analysis of a low-angle grain boundary in [001]-textured NiTi. (a) Bright field TEM image showing the low-angle grain boundary as a dislocation wall, with individual dislocations visible within the grains. (b, c) Selected area electron diffraction (SAED) patterns from the regions marked in (a). (d) Superelastic curves of both LPBF NiTi samples.

Additionally, Fig. 10(c) shows the composition of the O element in the bilayer oxide. The O 1s spectrum revealed two distinct peaks attributed to lattice oxide (O^{2-}) and hydroxide groups (OH^-), with binding energies of 530.1 eV and 531.8 eV, respectively. The highest content of O^{2-} is caused by the various Ti- and Ni-based oxides. However, the appearance of OH^- corresponds to the detected $Ni(OH)_2$.

To further characterize the corrosion behavior of the [001]-textured single-phase NiTi after electrochemical measurements, the microstructure was carefully analyzed. Fig. 11 provides insights into the corroded regions. In Fig. 11 (a), the corroded areas are observed to be primarily associated with small-size grains surrounded by high-angle grain boundaries, while the larger grains remain relatively unaffected. Fig. 11 (c) and 10 (d) display the orientation maps along the building direction (BD) and transverse direction (TD), respectively. Despite that grains grow along the BD, the adjacent grains show a large misorientation along the TD direction, which is characterized as high-angle grain boundaries (Fig. 11 (c) and 10(d)). Low-angle grain boundaries show limited corrosion compared to high-angle grain boundaries (Fig. 11 (c) and 10(d)). The KAM map in Fig. 11 (e) reveals localized strain at corroded high-angle boundaries, which aligns with the corroded regions (Fig. 11 (a) and 10(f)). This is because high-angle grain boundaries are high energy areas that are more prone to corrosion [38,39]. The phase map in Fig. 11 (g) confirms the single-phase B2 structure, underscoring that the enhanced corrosion resistance is also due to the absence of the martensitic phase, which was more susceptible to corrosion. These results indicate that the optimization of processing parameters not only improved microstructural homogeneity but also reduced susceptibility to corrosion process.

To study the preferential corrosion observed along the low-angle grain boundaries in the [001]-textured NiTi (Fig. 11), a focused ion beam (FIB)-machined lamella was prepared, including a representative low-angle grain boundary (details on the selection of the low-angle grain boundary are provided in the supplementary information and Figure S3). Fig. 12 (a) presents a TEM image of the low-angle grain boundary, clearly marked by a dislocation wall. The grain boundary consists of a dense arrangement of dislocations, while individual dislocations are also observed within the grains. The diffraction patterns in Fig. 12 (b) and (c), corresponding to the regions marked in Fig. 12 (a), confirm that the bicrystal grains on either side of the boundary share a near-[101] zone axis. This confirms the low-angle nature of the boundary. The dislocation structure within the low-angle grain boundary suggests that it is a high-energy region. Dislocations increase local lattice strain, leading to higher stored energy compared to the surrounding grain interiors. This localized energy concentration makes the low-angle grain boundary more susceptible to corrosion. Additionally, the dislocations can act as diffusion paths, accelerating the transport of corrosive agents and further contributing to the observed preferential corrosion [40,41]. While high-angle grain boundaries are generally more susceptible to corrosion due to their misorientation (Fig. 11), the presence of a dislocation wall in low-angle boundaries introduces a high-energy microstructural feature that makes these regions similarly vulnerable to corrosion.

The stress-strain curves in Fig. 12 (d) compare the superelasticity of LPBF [001]-textured single-phase NiTi with that of dual-phase NiTi. The [001]-textured NiTi exhibits superior superelastic performance, characterized by a higher stress plateau and recoverable strain compared to the dual-phase sample. Specifically, the [001]-textured sample shows a stress plateau starting at ~ 700 MPa with recoverable strains exceeding 5.5 %, while the dual-phase NiTi reaches lower plateau stresses (~ 600 MPa) and a smaller recoverable strain (~ 5 %).

The reduced hysteresis in the [001]-textured sample indicates improved energy efficiency during cyclic loading, which can be attributed to its homogeneous single-phase microstructure and the absence of stress concentrations at martensitic regions. In contrast, the dual-phase NiTi suffers from localized stress accumulation due to the presence of martensitic regions, resulting in lower overall performance.

4. Conclusions

This study demonstrates that the corrosion resistance of additively manufactured NiTi alloys can be significantly improved through tailored crystallographic texture, achieved by optimizing LPBF processing parameters. Dual-phase NiTi, composed of both austenitic and martensitic phases, exhibited localized corrosion susceptibility, with martensitic regions acting as anodic sites in chloride-rich environments. These findings were supported by potentiodynamic polarization testing and surface potential mapping, revealing the galvanic coupling between phases as a critical factor in corrosion behavior. The mechanisms underlying dual-phase formation were clarified through thermal simulations and microstructural analysis. Stress-induced phase transformation near melt pool boundaries during LPBF were identified as key contributors to martensite formation, driven by high thermal gradients.

By optimizing LPBF parameters, single-phase [001]-textured NiTi was successfully fabricated, eliminating martensitic regions and achieving substantial improvements in corrosion resistance and superelastic properties. Electrochemical testing revealed that the corrosion current of [001]-textured samples was only ~ 1 % of the original LPBF dual phase NiTi due to the formation of a more protective passive film, and enhanced surface stability. Moreover, the [001]-textured NiTi exhibited superior superelasticity, with a higher stress plateau, reduced hysteresis, and greater recoverable strain.

These findings reveal the critical role of crystallographic texture control in improving both the functional properties and corrosion resistance of NiTi alloys. Appropriate LPBF parameter adjustments offer a practical strategy for tailoring microstructures, paving the way for broader applications of NiTi in high-performance, corrosive, and functionally demanding environments.

CRedit authorship contribution statement

Zhu Jia-Ning: Writing – original draft, Validation, Software, Methodology, Investigation, Formal analysis, Conceptualization. **Li Ziyu:** Writing – original draft, Methodology, Investigation, Formal analysis, Data curation, Conceptualization. **Yan Zhaorui:** Writing – review & editing, Software, Methodology, Formal analysis, Data curation. **Rahimi Ehsan:** Formal analysis, Data curation. **Ding Zhaoying:** Writing – review & editing, Conceptualization. **Mol Arjan:** Writing – review & editing, Conceptualization. **Popovich Vera:** Writing – review & editing, Supervision, Project administration, Funding acquisition, Conceptualization.

Declaration of Competing Interest

The authors declare that they have no known competing financial interests or personal relationships that could have appeared to influence the work reported in this paper.

Acknowledgments

The authors are grateful to Dr. Evgenii Borisov at Peter the Great Saint-Petersburg Polytechnic University for the support with sample fabrication.

Appendix A. Supporting information

Supplementary data associated with this article can be found in the online version at [doi:10.1016/j.corsci.2025.112929](https://doi.org/10.1016/j.corsci.2025.112929).

Data availability

Data will be made available on request.

References

- [1] M. Elahinia, N. Shayesteh Moghaddam, M. Taheri Andani, A. Amerinatanzi, B. A. Bimber, R.F. Hamilton, Fabrication of NiTi through additive manufacturing: a review, *Prog. Mater. Sci.* 83 (2016) 630–663.
- [2] Z. Yan, J.-N. Zhu, E. Borisov, T. Riemslog, S.P. Scott, M. Hermans, J. Jovanova, V. Popovich, Superelastic response and damping behavior of additively manufactured Nitinol architected materials, *Addit. Manuf.* 68 (2023) 103505.
- [3] J.-N. Zhu, K. Liu, T. Riemslog, F.D. Tichelaar, E. Borisov, X. Yao, A. Popovich, R. Huizenga, M. Hermans, V. Popovich, Achieving superelasticity in additively manufactured Ni-lean NiTi by crystallographic design, *Mater. Des.* 230 (2023) 111949.
- [4] J. Zhu, X. Liang, V. Popovich, M. Hermans, I. Richardson, C. Bos, *Effic. Texture Predict. Addit. Manuf.* (2024).
- [5] J.-N. Zhu, E. Borisov, X. Liang, R. Huizenga, A. Popovich, V. Bliznuk, R. Petrov, M. Hermans, V. Popovich, Controlling microstructure evolution and phase transformation behavior in additively manufacturing of nitinol shape memory alloys by tuning hatch distance, *J. Mater. Sci.* (2022) 1–19.
- [6] J.P. Oliveira, A.J. Cavaleiro, N. Schell, A. Stark, R.M. Miranda, J.L. Ocana, F. M. Braz, Fernandes, Effects of laser processing on the transformation characteristics of NiTi: a contribute to additive manufacturing, *Scr. Mater.* 152 (2018) 122–126.
- [7] S. Saedi, N. Shayesteh Moghaddam, A. Amerinatanzi, M. Elahinia, H.E. Karaca, On the effects of selective laser melting process parameters on microstructure and thermomechanical response of Ni-rich NiTi, *Acta Mater.* 144 (2018) 552–560.
- [8] L. Xue, K.C. Atli, C. Zhang, N. Hite, A. Srivastava, A.C. Leff, A.A. Wilson, D. J. Sharar, A. Elwany, R. Arroyave, I. Karaman, Laser powder bed fusion of defect-free NiTi shape memory alloy parts with superior tensile superelasticity, *Acta Mater.* 229 (2022) 117781.
- [9] Y. Cao, X. Zhou, D. Cong, H. Zheng, Y. Cao, Z. Nie, Z. Chen, S. Li, N. Xu, Z. Gao, W. Cai, Y. Wang, Large tunable elastocaloric effect in additively manufactured Ni-Ti shape memory alloys, *Acta Mater.* 194 (2020) 178–189.
- [10] M. Beko, I. Knežević, N. Pudar, T. Dlačić, I. Š. Analysis of changes of NiTi alloys in different marine environments, in: 2022 21st International Symposium INFOTEH-JAHORINA (INFOTEH), 2022, pp. 1-5.
- [11] W. Predki, A. Knopik, B. Bauer, Engineering applications of NiTi shape memory alloys, *Mater. Sci. Eng., A* (2008) 481–482, 598-601.
- [12] P. Qiu, P. Gao, S. Wang, Z. Li, Y. Yang, Q. Zhang, Z. Xiong, S. Hao, Study on corrosion behavior of the selective laser melted NiTi alloy with superior tensile property and shape memory effect, *Corros. Sci.* 175 (2020) 108891.
- [13] G. Chen, S. Liu, C. Huang, Y. Ma, Y. Li, B. Zhang, L. Gao, B. Zhang, P. Wang, X. Qu, In-situ phase transformation and corrosion behavior of TiNi via LPBF, *Corros. Sci.* 203 (2022) 110348.
- [14] D. Gu, M. Chenglong, D. Donghua, Y. Jiankai, L. Kaijie, Z. Hongmei, H. Zhang, Additively manufacturing-enabled hierarchical NiTi-based shape memory alloys with high strength and toughness, *Virtual Phys. Prototyp.* 16 (2021). S19-S38.
- [15] G. Carlucci, L. Patriarcar, A.G. Demir, J.N. Lemke, A. Coda, B. Previtali, R. Casati, Building orientation and heat treatments effect on the pseudoelastic properties of NiTi produced by LPBF, *Shape Mem. Superelasticity* 8 (2022) 235–247.
- [16] Z. Yan, J.-N. Zhu, D. Hartl, T. Riemslog, S.P. Scott, R. Petrov, M. Hermans, J. Jovanova, V. Popovich, Correlation between microstructural inhomogeneity and architectural design in additively manufactured NiTi shape memory alloys, *Virtual Phys. Prototyp.* 19 (2024) e2396065.
- [17] M. Mousavi, E. Rahimi, J.M.C. Mol, Y. Gonzalez-Garcia, The effect of phosphorous content on the microstructure and localised corrosion of electroless nickel-coated copper, *Surf. Coat. Technol.* 492 (2024) 131174.
- [18] E. Rahimi, A. Rafsanjani-Abbasi, A. Imani, S. Hosseinpour, A. Davoodi, Correlation of surface volta potential with galvanic corrosion initiation sites in solid-state welded Ti-Cu bimetal using AFM-SKPFM, *Corros. Sci.* 140 (2018) 30–39.
- [19] E. Rahimi, A. Rafsanjani-Abbasi, A. Davoodi, S. Hosseinpour, Characterization of the native passive film on ferrite and austenite phases of sensitized 2205 duplex stainless steel, *J. Electrochem. Soc.* 166 (2019) C609.
- [20] A.B. Cook, Z. Barrett, S.B. Lyon, H.N. McMurray, J. Walton, G. Williams, Calibration of the scanning Kelvin probe force microscope under controlled environmental conditions, *Electrochim. Acta* 66 (2012) 100–105.
- [21] M. Rohwerder, F. Turcu, High-resolution Kelvin probe microscopy in corrosion science: scanning Kelvin probe force microscopy (SKPFM) versus classical scanning Kelvin probe (SKP), *Electrochim. Acta* 53 (2007) 290–299.
- [22] C. Senöz, S. Borodin, M. Stratmann, M. Rohwerder, In situ detection of differences in the electrochemical activity of Al₂Cu IMPs and investigation of their effect on FFC by scanning Kelvin probe force microscopy, *Corros. Sci.* 58 (2012) 307–314.
- [23] C. Örnek, D.L. Engelberg, Correlative EBSD and SKPFM characterisation of microstructure development to assist determination of corrosion propensity in grade 2205 duplex stainless steel, *J. Mater. Sci.* 51 (2016) 1931–1948.
- [24] A. Davoodi, J. Pan, C. Leygraf, S. Norgren, The role of intermetallic particles in localized corrosion of an aluminum alloy studied by SKPFM and integrated AFM/SECM, *J. Electrochem. Soc.* 155 (2008) C211.
- [25] C. Örnek, D.L. Engelberg, SKPFM measured volta potential correlated with strain localisation in microstructure to understand corrosion susceptibility of cold-rolled grade 2205 duplex stainless steel, *Corros. Sci.* 99 (2015) 164–171.
- [26] M. Sarvghad-Moghaddam, R. Parvizi, A. Davoodi, M. Haddad-Sabzevar, A. Imani, Establishing a correlation between interfacial microstructures and corrosion initiation sites in Al/Cu joints by SEM-EDS and AFM-SKPFM, *Corros. Sci.* 79 (2014) 148–158.
- [27] J. Frenzel, E.P. George, A. Dlouhy, C. Somsen, M.F.X. Wagner, G. Eggeler, Influence of Ni on martensitic phase transformations in NiTi shape memory alloys, *Acta Mater.* 58 (2010) 3444–3458.
- [28] T. DeRoy, H.L. Wei, J.S. Zuback, T. Mukherjee, J.W. Elmer, J.O. Milewski, A. M. Beese, A. Wilson-Heid, A. De, W. Zhang, Additive manufacturing of metallic components – process, structure and properties, *Prog. Mater. Sci.* 92 (2018) 112–224.
- [29] M. Liu, J.-N. Zhu, V.A. Popovich, E. Borisov, J.M.C. Mol, Y. Gonzalez-Garcia, Passive film formation and corrosion resistance of laser-powder bed fusion fabricated NiTi shape memory alloys, *J. Mater. Res. Technol.* 23 (2023) 2991–3006.
- [30] H.-H. Ge, G.-D. Zhou, W.-Q. Wu, Passivation model of 316 stainless steel in simulated cooling water and the effect of sulfide on the passive film, *Appl. Surf. Sci.* 211 (2003) 321–334.
- [31] M. Wang, Z. Zhou, Q. Wang, L. Wu, Z. Wang, X. Zhang, Long term semiconducting and passive film properties of a novel dense FeCrMoCBY amorphous coating by atmospheric plasma spraying, *Appl. Surf. Sci.* 495 (2019) 143600.
- [32] W. Niu, R.S. Lillard, Z. Li, F. Ernst, Properties of the passive film formed on interstitially hardened AISI 316L stainless steel, *Electrochim. Acta* 176 (2015) 410–419.
- [33] A. Shanaghi, P.K. Chu, Enhancement of mechanical properties and corrosion resistance of NiTi alloy by carbon plasma immersion ion implantation, *Surf. Coat. Technol.* 365 (2019) 52–57.
- [34] L. Jinlong, L. Tongxiang, W. Chen, D. Limin, Surface corrosion enhancement of passive films on NiTi shape memory alloy in different solutions, *Mater. Sci. Eng.: C* 63 (2016) 192–197.
- [35] L. Wang, H. Yu, S. Wang, B. Chen, Y. Wang, W. Fan, D. Sun, Quantitative analysis of local fine structure on diffusion of point defects in passive film on Ti, *Electrochim. Acta* 314 (2019) 161–172.
- [36] M.T. Greiner, Z.-H. Lu, Thin-film metal oxides in organic semiconductor devices: their electronic structures, work functions and interfaces, *NPG Asia Mater.* 5 (2013) e55-e55.
- [37] J. Gong, W. Luo, Y. Zhao, J. Wang, S. Wang, C. Hu, J. Yang, Y. Dai, Surface engineering of Ni wires and rapid growth strategy of Ni-MOF synergistically contribute to high-performance fiber-shaped aqueous battery, *Small* 18 (2022) 2204346.
- [38] J. Zhang, L. Xu, Y. Han, L. Zhao, B. Xiao, New perspectives on the grain boundary misorientation angle dependent intergranular corrosion of polycrystalline nickel-based 625 alloy, *Corros. Sci.* 172 (2020) 108718.
- [39] J. Yan, N.M. Heckman, L. Velasco, A.M. Hodge, Improve sensitization and corrosion resistance of an Al-Mg alloy by optimization of grain boundaries, *Sci. Rep.* 6 (2016) 26870.
- [40] B. Liu, X. Zhang, X. Zhou, T. Hashimoto, J. Wang, The corrosion behaviour of machined AA7150-T651 aluminium alloy, *Corros. Sci.* 126 (2017) 265–271.
- [41] D.J. Sprouster, W. Streit Cunningham, G.P. Halada, H. Yan, A. Pattammattel, X. Huang, D. Olds, M. Tilton, Y.S. Chu, E. Dooryhee, G.P. Manogharan, J. R. Trelewicz, Dislocation microstructure and its influence on corrosion behavior in laser additively manufactured 316L stainless steel, *Addit. Manuf.* 47 (2021) 102263.